



## NRC Publications Archive Archives des publications du CNRC

### **Accelerated removal of Fe-antisite defects while nanosizing hydrothermal $\text{LiFePO}_4$ with $\text{Ca}^{2+}$**

Paolella, Andrea; Turner, Stuart; Bertoni, Giovanni; Hovington, Pierre;  
Flacau, Roxana; Boyer, Chad; Feng, Zimin; Colombo, Massimo; Marras,  
Sergio; Prato, Mirko; Manna, Liberato; Guerfi, Abdelbast; Demopoulos,  
George P.; Armand, Michel; Zaghib, Karim

This publication could be one of several versions: author's original, accepted manuscript or the publisher's version. /  
La version de cette publication peut être l'une des suivantes : la version prépublication de l'auteur, la version  
acceptée du manuscrit ou la version de l'éditeur.

For the publisher's version, please access the DOI link below. / Pour consulter la version de l'éditeur, utilisez le lien  
DOI ci-dessous.

#### **Publisher's version / Version de l'éditeur:**

<https://doi.org/10.1021/acs.nanolett.6b00334>

*Nano Letters*, 16, 4, pp. 2692-2697, 2016-03-11

#### **NRC Publications Record / Notice d'Archives des publications de CNRC:**

<https://nrc-publications.canada.ca/eng/view/object/?id=9c4e096d-0c16-4cab-a2cd-5894bdc25dec>

<https://publications-cnrc.canada.ca/fra/voir/objet/?id=9c4e096d-0c16-4cab-a2cd-5894bdc25dec>

Access and use of this website and the material on it are subject to the Terms and Conditions set forth at

<https://nrc-publications.canada.ca/eng/copyright>

READ THESE TERMS AND CONDITIONS CAREFULLY BEFORE USING THIS WEBSITE.

L'accès à ce site Web et l'utilisation de son contenu sont assujettis aux conditions présentées dans le site

<https://publications-cnrc.canada.ca/fra/droits>

LISEZ CES CONDITIONS ATTENTIVEMENT AVANT D'UTILISER CE SITE WEB.

**Questions?** Contact the NRC Publications Archive team at

PublicationsArchive-ArchivesPublications@nrc-cnrc.gc.ca. If you wish to email the authors directly, please see the  
first page of the publication for their contact information.

**Vous avez des questions?** Nous pouvons vous aider. Pour communiquer directement avec un auteur, consultez la  
première page de la revue dans laquelle son article a été publié afin de trouver ses coordonnées. Si vous n'arrivez  
pas à les repérer, communiquez avec nous à PublicationsArchive-ArchivesPublications@nrc-cnrc.gc.ca.



National Research  
Council Canada

Conseil national de  
recherches Canada

Canada

# Accelerated Removal of Fe-Antisite Defects while Nanosizing Hydrothermal $\text{LiFePO}_4$ with $\text{Ca}^{2+}$

Andrea Paoletta,<sup>†</sup> Stuart Turner,<sup>‡</sup> Giovanni Bertoni,<sup>§</sup> Pierre Hovington,<sup>†</sup> Roxana Flacau,<sup>||</sup> Chad Boyer,<sup>||</sup> Zimin Feng,<sup>†</sup> Massimo Colombo,<sup>⊥</sup> Sergio Marras,<sup>⊥</sup> Mirko Prato,<sup>⊥</sup> Liberato Manna,<sup>⊥</sup> Abdelbast Guerfi,<sup>†</sup> George P. Demopoulos,<sup>#</sup> Michel Armand,<sup>▽</sup> and Karim Zaghib<sup>\*,†</sup>

<sup>†</sup>IREQ—Institute Recherche d'Hydro-Québec, 1800 Boulevard Lionel Boulet, Varennes, QC J3X 1S1, Canada

<sup>‡</sup>EMAT, University of Antwerp, Groenenborgerlaan 171, BE 2020, Antwerp, Belgium

<sup>§</sup>IMEM—CNR, Parco Area delle Scienze 37/A, 43124 Parma, Italy

<sup>||</sup>National Research Council of Canada, Chalk River Laboratories, Chalk River, Ontario K0J 1J0, Canada

<sup>⊥</sup>Istituto Italiano di Tecnologia, via Morego 30, 16130 Genova, Italy

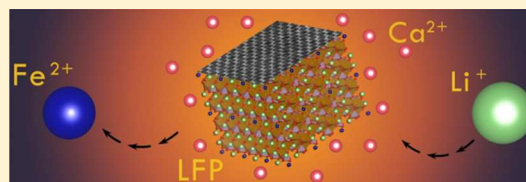
<sup>#</sup>Mining and Materials Engineering Department, McGill University, Wong Building, 3610 University Street, Montreal, QC H3A 0C5, Canada

<sup>▽</sup>CIC energigune—Parque Tecnológico, C/Albert Einstein 48, CP 01510 Miñano, Alava, Spain

## Supporting Information

**ABSTRACT:** Based on neutron powder diffraction (NPD) and high angle annular dark field scanning transmission electron microscopy (HAADF-STEM), we show that calcium ions help eliminate the Fe-antisite defects by controlling the nucleation and evolution of the  $\text{LiFePO}_4$  particles during their hydrothermal synthesis. This Ca-regulated formation of  $\text{LiFePO}_4$  particles has an overwhelming impact on the removal of their iron antisite defects during the subsequent carbon-coating step since (i) almost all the Fe-antisite defects aggregate at the surface of the  $\text{LiFePO}_4$  crystal when the crystals are small enough and (ii) the concomitant increase of the surface area, which further exposes the Fe-antisite defects. Our results not only justify a low-cost, efficient and reliable hydrothermal synthesis method for  $\text{LiFePO}_4$  but also provide a promising alternative viewpoint on the mechanism controlling the nanosizing of  $\text{LiFePO}_4$ , which leads to improved electrochemical performances.

**KEYWORDS:** Antisite,  $\text{LiFePO}_4$ , calcium, surface, defects, hydrothermal



Since the early development of  $\text{LiFePO}_4$ ,<sup>1</sup> great efforts have been dedicated to the study of this material due to its superior safety, high stability, and suitable operating voltage ( $\sim 3.4$  V). Olivine  $\text{LiFePO}_4$  has a  $Pnma$  structure with lithium ions confined in the channels (M1 site) formed by interconnecting  $\text{FeO}_6$  octahedra (M2 site) and  $\text{PO}_4$  tetrahedra. Among all the proposed synthesis methods,<sup>2–5</sup> the hydrothermal route is likely the cheapest one to prepare  $\text{LiFePO}_4$ . However, this method leads to a large fraction of Fe-antisite defects in the final product, and there is, to date, no procedure that can avoid their formation when using the hydrothermal approach.<sup>6,7</sup> According to current understanding, the Fe-antisite defects can be slowly reduced only by long synthesis time (5–7 h at 180–200 °C),<sup>8</sup> the use of alcoholic solvents (ethylene glycol or ethanol) instead of water<sup>9,10</sup> or by annealing at high temperature ( $T > 600$  °C).<sup>2</sup> The important studies of Graetz (via in situ X-ray diffraction),<sup>11,12</sup> Iversen (via neutron powder diffraction)<sup>13</sup> and Ikuhara (via HAADF-STEM)<sup>14</sup> demonstrated that the Fe-antisite defects are formed by Fe-ions located in M1 sites and block the  $\text{Li}^+$  diffusion pathway. The Fe-antisite defects are known to be located mainly at the surface of the crystals<sup>15</sup> and can be largely eliminated during the

synthesis by a slow cation exchange reaction with a Li-rich amorphous layer that is in close contact with the crystal. In this work we show that calcium ions can facilitate an efficient and complete removal of Fe-antisite defects. This procedure works in two steps: (i) by the addition of calcium sulfate to the starting mix we observed the formation of nanocrystals at the early stage of the hydrothermal synthesis of  $\text{LiFePO}_4$  in contrast to micron size crystals as reported previously;<sup>15</sup> (ii) since the Fe-antisite defects aggregate at the surface of the crystals, a subsequent carbon coating procedure can completely remove the defects. Regardless of the presence of calcium, the Fe-antisite defects always aggregate mainly at the crystal surface. The effects of calcium ions are, on the one hand, to regulate the nucleation and limit the growth of LFP particles to nanometer scale and, on the other hand, to promote the aggregation of the Fe-antisite defects at the surface.

**Results and Discussion.** In this work we compared two different hydrothermally synthesized  $\text{LiFePO}_4$  samples: the

**Received:** January 26, 2016

**Revised:** March 2, 2016

**Published:** March 11, 2016

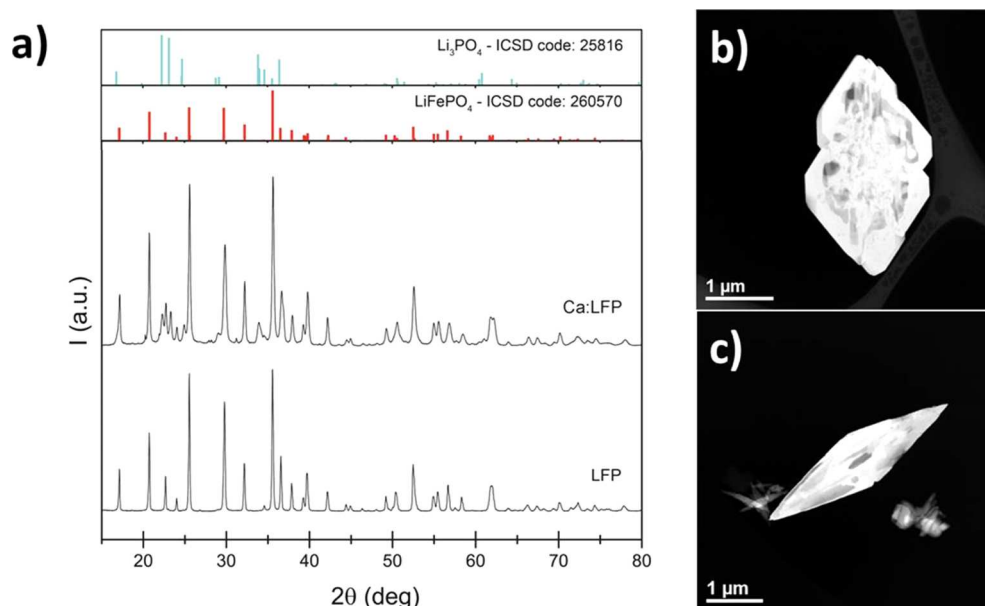


**Figure 1.** (a) XRD patterns, (b) STEM image of standard hydrothermal LFP, and (c) STEM image of calcium modified hydrothermal LFP.

classical hydrothermal  $\text{LiFePO}_4$  (named LFP) and the calcium ion mediated hydrothermal  $\text{LiFePO}_4$  synthesis (named Ca:LFP). LFP and Ca:LFP were synthesized following the recipe described in the [Materials and Methods](#) section. We analyzed four different intermediates collected at different times: 10 min, 15 min, 30 min, and 5 h (see [Materials and Methods](#) section). We investigated the LFP and Ca:LFP samples after 15 min of synthesis. The samples were analyzed via XRD and HAADF-STEM measurements (see [Figure 1](#)). The shapes of the crystals synthesized with the two methods are distinctly different. The LFP sample at 15 min is in the form of micron-sized hexagonal hollow crystal, with a 4 nm thick amorphous layer as previously reported.<sup>15</sup> The Ca:LFP sample instead is in the form of rhombic crystal, with an average amorphous layer of only 1 nm thick (see [Figure S1](#) in [SI](#)).

Also, the Ca:LFP sample shows a homogeneous distribution of calcium inside the  $\text{LiFePO}_4$  crystals (see [Figure 2](#)): the total amount of calcium ions inside  $\text{LiFePO}_4$  being only around 0.1–0.3%, as determined by EDS. These data are consistent with compositional analysis by time of flight secondary ion mass spectroscopy (TOF-SIMS) (see [Figure S4](#) in [SI](#)). According to the XRD measurements,  $\text{Li}_3\text{PO}_4$  and  $\beta\text{-Ca}_3(\text{PO}_4)_2$  were detected as impurities. The observation of calcium phosphate segregation from olivine  $\text{LiFePO}_4$  is in agreement with paleographic findings<sup>16</sup> and melt casting synthesis,<sup>17</sup> while other bivalent ions like  $\text{Mg}^{2+}$ ,  $\text{Mn}^{2+}$ ,  $\text{Co}^{2+}$ , and  $\text{Ni}^{2+}$  easily form solid solutions.<sup>2</sup> Also, XRD analysis helped to shed light on the formation and growth mechanism of Ca:LFP (see [Materials and Methods](#) section and [SI](#)): after 10 min of synthesis,  $\text{NH}_4\text{LiSO}_4$ ,  $\text{Li}_3\text{PO}_4$ , and  $\beta\text{-Ca}_3(\text{PO}_4)_2$  phases were detected (see [Figure S2](#) in [SI](#)), while only a tiny amount of  $\text{LiFePO}_4$  was present. Considering (i) the formation of  $\text{Li}_3\text{PO}_4$  and  $\beta\text{-Ca}_3(\text{PO}_4)_2$  as first intermediate instead of vivianite;<sup>15</sup> (ii) the gradual disappearance of  $\text{Li}_3\text{PO}_4$  and  $\beta\text{-Ca}_3(\text{PO}_4)_2$  and the formation of  $\text{LiFePO}_4$ ; (iii) the presence of residual Ca inside the crystal (see [Figure 2](#) and [Figure S4](#) in [SI](#)); and (iv) the presence of Ca-rich phase around  $\text{LiFePO}_4$ , we suggest that  $\text{LiFePO}_4$  is formed by gradual reaction of  $\text{Fe}^{2+}$  with a lithium–calcium based phosphate precursor (e.g.,  $\text{LiCa}_{10}(\text{PO}_4)_7$  see

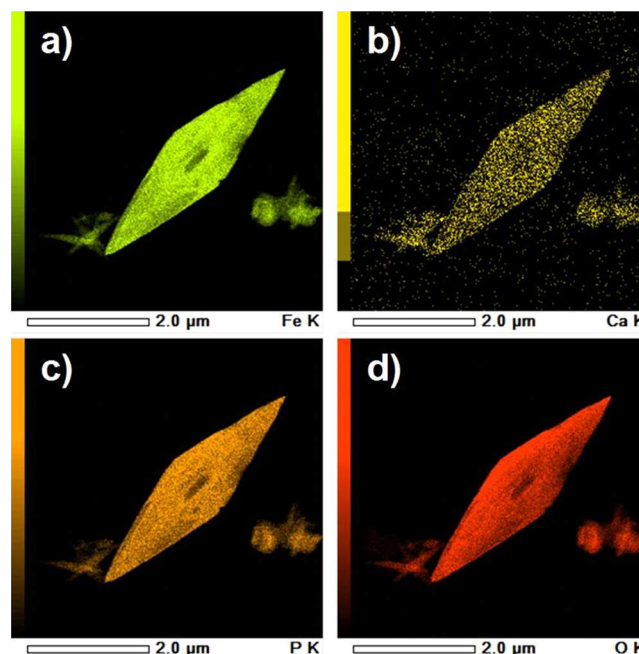


**Figure 2.** EDS image mapping on hydrothermal Ca:LFP sample showing the homogeneous distribution of (a) iron, (b) calcium, (c) phosphorus, and (d) oxygen ions inside Ca: $\text{LiFePO}_4$  crystals.

simulations in [SI](#)). We believe this proposed reaction pathway can be partially supported by our first-principles calculations (see [Materials and Methods](#) section and [SI](#)). With equal amount of atoms,  $\text{Li}_3\text{PO}_4$  plus  $\text{Ca}_3(\text{PO}_4)_2$  has higher total electronic energy than  $\text{LiCaPO}_4$ . An exchange of cations  $\text{Ca}^{2+}$  with  $\text{Fe}^{2+}$  in dilute aqueous solutions is also energetically favored. Due to the fact that ion-exchanging intercalation reactions happen much more slowly than the other reactions, we explained the existence of  $\text{LiCaPO}_4$  as an intermediate product.

The Ca:LFP crystals are mainly composed of smaller nanocrystals that are assembled in a rhombic structure as shown in [Figure 3a,b](#). Brunauer–Emmett–Teller (BET)



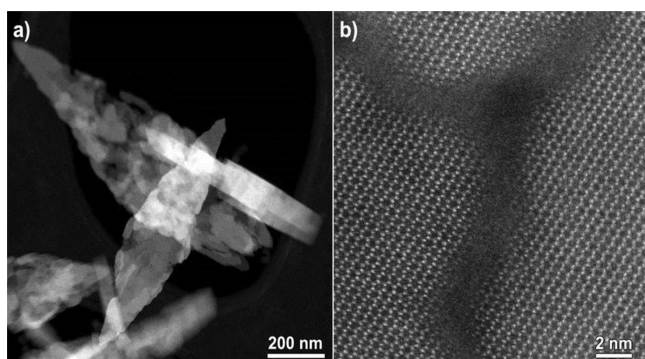


**Figure 3.** (a) HAADF-STEM image of the porous  $\text{LiFePO}_4$  crystals and (b) high resolution HAADF-STEM image of amorphous regions within individual crystals (synthesis made using 3% of calcium ions and 15 min of synthesis).

analysis (see Table 1) highlights a significant increase of the surface area at 15 min in the presence of Ca ( $19 \text{ m}^2/\text{g}$  for

**Table 1.** Surface Area of LFP and Ca:LFP Samples by BET Analysis

sample	surface area [ $\text{m}^2/\text{g}$ ]			
	15 min	30 min	5 h	15 min-carbon coated
LFP (ref <sup>15</sup> )	7.3	6.2	5.4	4.2
Ca:LFP	19.1	9.1	4.6	17.4

Ca:LFP vs  $7.3 \text{ m}^2/\text{g}$  for LFP sample), consistent with a smaller average dimension of the crystals at this stage of the synthesis. At 30 min the Ca:LFP crystals have a surface area of  $9.1 \text{ m}^2/\text{g}$ , while the LFP crystals only  $6.3 \text{ m}^2/\text{g}$ . Finally after 5 h of synthesis the surface areas become comparable ( $\sim 5 \text{ m}^2/\text{g}$ ).

According to NPD, the evolution of Fe-antisites during crystal formation was the following (see Materials and Methods section and corresponding refinements in SI): at 15 min the percentage of Fe-antisites exhibited by these two samples was almost the same: 7–8% of Fe atoms in M1. After 30 min of synthesis, 4% of Fe atoms were in M1 sites in the LFP<sup>15</sup> sample compared to 1% for the Ca:LFP sample. Only after 5 h of synthesis, the percentage of Fe-antisites for the two samples was found once again comparable ( $\sim 1$ –2%).<sup>15</sup> HAADF-STEM analysis (Figure 4) showed that the standard hydrothermal LFP sample (without calcium) after 15 min of synthesis exhibits a higher percentage of Fe-antisites in the bulk compared to the Ca:LFP sample (see Figure 4a,b) in which the Fe-antisites were more densely confined at the surface (see Figure 4c,d). After 15 min of synthesis, the presence of calcium did not alter the percentage of the Fe-antisite defects but promoted the formation of nanoparticles (instead of micron-sized particles) with a higher density of Fe-antisite defects at their surface. As such, the calcium ions favor the formation of high surface  $\text{LiFePO}_4$  crystals in which the Fe-antisite defects are aggregated on a thin surface layer compared to LFP crystals synthesized without calcium additive (Figure 4e). We conclude that during synthesis the formation of nanoparticles by the action of calcium ions accelerates the elimination of Fe-antisites in comparison with the classical LFP synthesis: in the presence of Ca, the percentage of Fe-antisites was reduced from 8% after 15 min to  $\sim 1$ –2% at 30 min, instead of 4% as previously reported for the classical Ca-free  $\text{LiFePO}_4$  synthesis.<sup>15</sup>

After carbon coating of the samples (see Materials and Methods section and XRD patterns in Figure S3 of SI) we performed electrochemical tests. After 15 min the LFP sample exhibited a capacity of only 40 mAh/g at C/12 and 30 mAh/g at 10C (see Figure 5a,b), while the Ca:LFP had a capacity of 120 mAh/g at C/12 and 70 mAh/g at 10C. The addition of

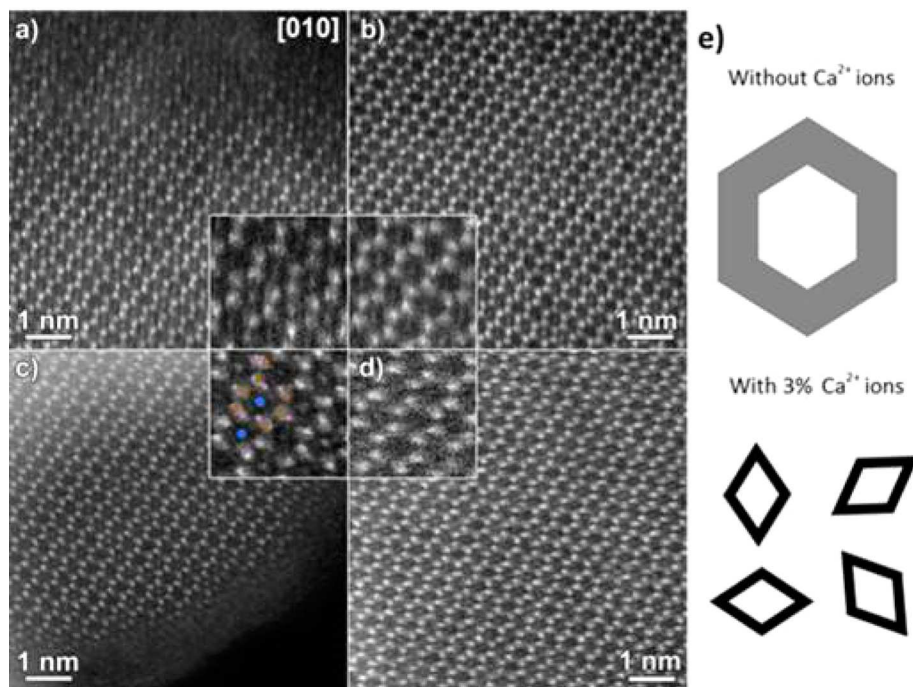


**Figure 4.** High-resolution HAADF-STEM images of Fe-antisite defects in (a) surface and (b) bulk of LFP; (c) surface and (d) bulk of Ca:LFP. Inset: enlarged regions of panels a–d with an overlaid structural model with Fe in brown, P in purple, and the Li antisite position in blue (oxygen positions are not shown for clarity) in panel c. (e) Antisite distribution models for LFP and Ca:LFP.

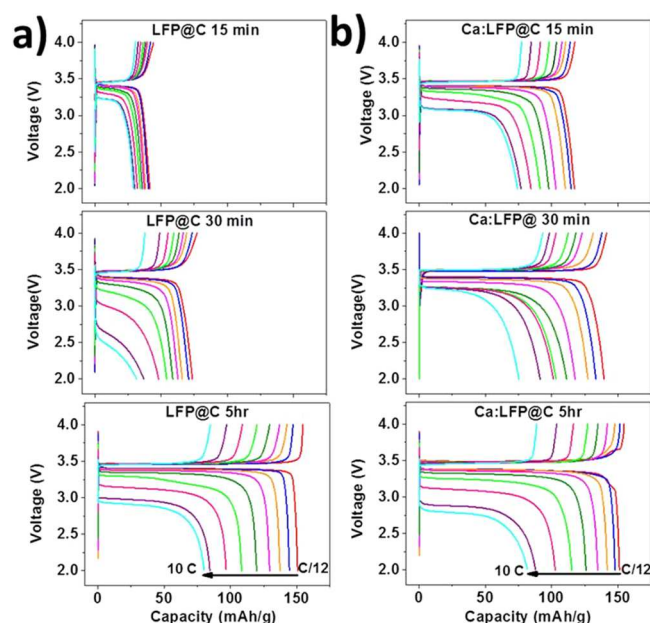


**Figure 5.** Charge/discharge curves at different C rate for (a) LiFePO<sub>4</sub> without calcium and (b) LiFePO<sub>4</sub> with 3% of calcium after 15 min, 30 min, and 5 h of synthesis. The discharge rate C/12 is in red, C/8 in blue, C/4 in orange, C/2 in magenta, 1C in olive green, 2C in green, 4C in pink, 8C in purple, and 10C in cyan.

calcium strongly improved the performance at this stage. It must be noted that, in the Ca:LFP sample Li<sub>3</sub>PO<sub>4</sub> was still present as impurity (see Figure S3).

According to the XRD, the as-synthesized LFP sample collected after 15 min was composed of pure LiFePO<sub>4</sub>, while NPD revealed the presence of 7–8% of Fe-atoms in M1 sites. The same percentage of Fe-antisite defects was detected on the as-synthesized Ca:LFP sample after 15 min. Therefore, the two samples have the same amount of defects at the early stages of the synthesis. For LFP (without calcium), the sample after carbon coating was characterized by a reduction in the percentage of the Fe-antisite defects, which dropped from 8% to 3.5%. These observations indicate that the antisite defects are not completely eliminated by the annealing treatment; instead a fraction of them is simply relocated out of the crystal forming new impurities (Fe<sub>2</sub>P<sub>2</sub>O<sub>7</sub>, see Figure S11 in SI). The percentage of antisite defects in the Ca:LFP sample after the carbon coating step was instead negligible (see SI for more details). We also observed the formation of Fe<sub>2</sub>P<sub>2</sub>O<sub>7</sub> in this case, while no Fe<sub>2</sub>P<sub>2</sub>O<sub>7</sub> was observed in the LFP@C sample (Fe-antisite defect free) obtained after 5 h of synthesis. This impurity was already detected after carbon coating by Wang et al.<sup>18</sup> at the surface of LiFePO<sub>4</sub> and recently by Masquelier et al.<sup>19</sup> in deficient Li-ion LiFePO<sub>4</sub> structure. These results are in agreement with the observations by HAADF-STEM imaging (Figure 6). In the case of LFP, Fe-antisite defects were still observed at the surface of the crystals (see Figure 6b), while no Fe-antisite defects at the surface were detected on Ca:LFP crystals (Figure 6a). Moreover along the [010] orientation in LFP crystals (without calcium), we observed the epitaxial growth of magnetite Fe<sub>3</sub>O<sub>4</sub> nanoparticles (see Figure S17). One conclusion that can be drawn from these data is that the initial surface area becomes a key parameter in order to remove Fe-antisites facilitating the intercalation/deintercalation process of lithium ions.

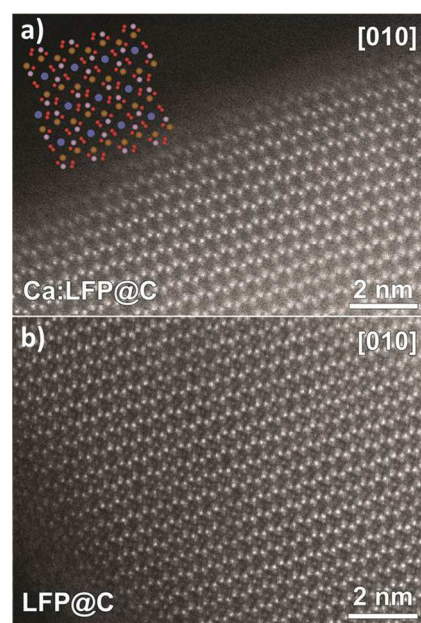


**Figure 6.** (a) HAADF-STEM image of 3% Ca-LFP@C showing an absence of Fe-antisites at the surface with an overlaid structural model with Fe in brown, P in purple, the Li antisite position in blue, and oxygen positions in red. (b) HAADF-STEM image of LFP@C showing the presence of Fe-antisites at the surface.

The middle panels of Figure 5 refer to samples prepared with a 30 min synthesis followed by a carbon coating step: the LFP sample evidenced 75 mAh/g capacity at C/12 and only 25 mAh/g capacity at 10C. However, the Ca:LFP sample exhibited much higher capacities: 140 mAh/g at C/12 and 75 mAh/g at 10C. The two pristine samples have a different percentage of Fe-antisite defects and different surface area values: the classical LFP sample had 4% of antisite defects<sup>15</sup> and a surface area of 6.2 m<sup>2</sup>/g, while Ca:LFP had ~1% of antisite defects (see SI) and a surface area of 9.1 m<sup>2</sup>/g, thus an increase of ~50%. The removal of Fe-antisites during the synthesis and by carbon coating step is clearly facilitated by nanosizing of LFP. The performances of Ca:LFP after 30 min of synthesis were comparable to those of the Ca:LFP sample with 10% of calcium after 5 h of synthesis (see synthesis in Materials and Methods section and Figures S2 and S18) due the presence of residual  $\beta$ -Ca<sub>3</sub>(PO<sub>4</sub>)<sub>2</sub> as impurity.

The 5 h LFP and Ca:LFP samples had the same percentage of antisite defects and the same surface area and they exhibited comparable electrochemical performances (see Figure 5), in agreement with the literature.<sup>20,21</sup> Electrochemical impedance spectra (EIS, in the form of Nyquist plots) of the LFP@C and Ca:LFP@C electrodes at the fully lithiated state (LiFePO<sub>4</sub>) after 15 min, 30 min, and 5 h of synthesis are reported in Figure S19. In the spectra the intercept on the real axis (Z real) corresponds to the electrolyte resistance (Re), and the semicircle in the middle of the high-frequency region (100 to 1 kHz) is related to the charge transfer resistance (R<sub>ct</sub> ≈ 50–150 Ω) for the Li transfer across the crystals electrode/electrolyte interface. After 15 min LFP@C and Ca:LFP@C exhibited a comparable charge transfer resistance that is probably due to the presence of high amount of lithium at the surface compared to 30 min and 5 h LFP samples.<sup>15</sup> After 30 min and 5 h of synthesis the Ca:LFP@C (blue curves) sample exhibited a charge transfer resistance that was lower



than LFP@C (red curves), mainly due to the improvement of electronic conductivity for Ca-sample after Fe-antisites removal. As control experiments, to confirm the unique behavior of calcium ions in LFP hydrothermal synthesis, we replaced  $\text{Ca}^{2+}$  with  $\text{Mg}^{2+}$  (being magnesium a metal alkaline earth as calcium as well) in 15 min synthesis (see [Materials and Methods](#) section for more details). According to XRD measurement (see [Figure S4](#))  $\text{Li}_{0.95}\text{Mg}_{0.05}\text{FePO}_4$  was detected (with  $\text{Mg}^{2+}$  ions occupying M1 sites). By EDS and TOF-SIMS we observed a homogeneous distribution of  $\text{Mg}^{2+}$  ions inside the crystals (Mg around 3% vs Fe) meaning a good solubility of magnesium ions inside the olivine structure in agreement with Whittigham et al. results<sup>2</sup> (see [Figures S5 and S8](#)). By XRD and mapping, no Mg-rich phosphate crystals were detected. The surface area of the particles is  $3.4 \text{ m}^2/\text{g}$  (much lower than Ca:LFP particles at this stage). We then performed carbon coatings, followed by electrochemical tests: the performance of the sample is very poor ( $\sim 40 \text{ mAh/g}$  at C/12, see [Figure S20](#)). These results confirm the uniqueness of calcium ions in hydrothermal  $\text{LiFePO}_4$  synthesis due to their low solubility in olivine structure.

In conclusion, beyond the known benefits of  $\text{LiFePO}_4$  nanosizing,<sup>22</sup> the nucleation path, in this case regulated by the presence of calcium ions, strongly contributes to the removal of Fe-antisite defects at the surface of small LFP crystals. These results are in agreement with recent studies of Tao's group<sup>23</sup> according to which the Fe-antisite defects tend to aggregate and the denser aggregation is at the surface, which helps their elimination. The addition of calcium sulfate as additive could be industrially relevant in order to develop a faster and therefore low cost hydrothermal synthesis of  $\text{LiFePO}_4$  by favoring the effective elimination of antisite defects via segregation in a thinner surface layer.

**Materials and Methods. Chemicals.** Iron sulfate heptahydrate  $\text{FeSO}_4 \cdot 7\text{H}_2\text{O}$  (purity  $\geq 99.0\%$ ), calcium sulfate dihydrate (purity  $\geq 99.0\%$ ), magnesium sulfate anhydrous  $\text{MgSO}_4$ , lithium hydroxide monohydrate  $\text{LiOH} \cdot \text{H}_2\text{O}$  (purity  $\geq 98.0\%$ ), phosphoric acid  $\text{H}_3\text{PO}_4$  (85% w/w in water,  $\geq 99.9\%$  trace metals basis), ammonium hydroxide  $\text{NH}_4\text{OH}$  (solution 28.0–30.0%  $\text{NH}_3$  basis), and ascorbic acid  $\text{C}_6\text{H}_8\text{O}_6$  (purity  $\geq 99.0\%$ ) were purchased by Sigma-Aldrich.

**Hydrothermal Synthesis of  $\text{LiFePO}_4$  (LFP).** In a standard hydrothermal synthesis 33.6 g (0.12 mol) of  $\text{FeSO}_4 \cdot 7\text{H}_2\text{O}$ , 15.41 g (0.36 mol) of  $\text{LiOH} \cdot \text{H}_2\text{O}$ , and 13.83 g (0.12 mol) of  $\text{H}_3\text{PO}_4$ , 0.5 g of ascorbic acid ( $\text{C}_6\text{H}_8\text{O}_6$ ) are mixed with 300 mL of deionized water in a glass liner. The final molar ratio between  $\text{Li}/\text{Fe}/\text{PO}_4/\text{C}_6\text{H}_8\text{O}_6$  was 3:1:1:0.008. The pH was controlled at 7.8 by dropwise addition of ammonium hydroxide  $\text{NH}_4\text{OH}$ . The synthesis was performed in a stirred autoclave (OM-JAPAN). We collected intermediates at different times in the heating ramp (from RT to  $180^\circ\text{C}$  in 30 min): after 15 min ( $120^\circ\text{C}$ ) and after 30 min (intermediate at the end of the heating ramp, the temperature was  $180^\circ\text{C}$ ). Then the last sample was collected after 5 h at  $180^\circ\text{C}$ .

**Hydrothermal Synthesis of 3% Ca: $\text{LiFePO}_4$  (Ca:LFP).** To the synthesis described above was added  $\text{CaSO}_4 \cdot 2\text{H}_2\text{O}$ ; 32.68 g (0.1164 mol) of  $\text{FeSO}_4 \cdot 7\text{H}_2\text{O}$  is mixed with 0.62 g (0.0036 mol) of  $\text{CaSO}_4 \cdot 2\text{H}_2\text{O}$ . The total amount of mol of bivalent cation (calcium and iron) is kept fixed at 0.12 mol. The pH was controlled at 7.8 by dropwise addition of ammonium hydroxide  $\text{NH}_4\text{OH}$ . The synthesis is performed in a stirred autoclave (OM-JAPAN). We collected intermediates at different times in the heating ramp (from RT to  $180^\circ\text{C}$  in 30 min): after 10 min

of synthesis (at the temperature approximately of  $90^\circ\text{C}$ ), after 15 min ( $120^\circ\text{C}$ ), and after 30 min (intermediate at the end of the heating ramp, the temperature was  $180^\circ\text{C}$ ). Then the last sample was collected after 5 h at  $180^\circ\text{C}$ . For the 5 h synthesis of Ca: $\text{LiFePO}_4$  with 10% of calcium we used 30.02 g (0.108 mol) of  $\text{FeSO}_4 \cdot 7\text{H}_2\text{O}$  and 2.06 g (0.0036 mol) of  $\text{CaSO}_4 \cdot 2\text{H}_2\text{O}$ .

**Hydrothermal Synthesis of 3% Mg: $\text{LiFePO}_4$  (Mg:LFP), 15 min.** To the synthesis described above was added  $\text{MgSO}_4$ ; 32.68 g (0.1164 mol) of  $\text{FeSO}_4 \cdot 7\text{H}_2\text{O}$  is mixed with 0.72 g (0.0036 mol) of  $\text{MgSO}_4$ . The total amount of mol of bivalent cation (Magnesium and Iron) is kept fixed at 0.12 mol. The pH was controlled at 7.8 by dropwise addition of ammonium hydroxide  $\text{NH}_4\text{OH}$ . The synthesis was performed in a stirred autoclave (OM-JAPAN) for 15 min reaching approximately a temperature of  $120^\circ\text{C}$ .

**Carbon Coating and Electrode Preparation.** For all the samples 5.66 g of a lactose aqueous solution (10% w/w) was mixed with 5 g of  $\text{LiFePO}_4$  for 30 min (5 g of powder including all the possible impurities). Then the final slurry was annealed in a carbon boat at  $95^\circ\text{C}$  overnight and then annealed at  $700^\circ\text{C}$  for 3 h under nitrogen. The  $\text{LiFePO}_4$  sample carbon coated (89% w/w) was mixed with Denka Carbon (3%), VGCF (3%), and PVDF (5%) and *N*-methyl pyrrolidone (NMP) as solvent. After mixing with SPEX the final slurry was laminated on aluminum foil. Initially the electrode was dried for 24 h at  $75^\circ\text{C}$  under nitrogen flow just to remove NMP. After lamination and punching, the electrode was dried at  $120^\circ\text{C}$  for 5 h under vacuum.

**X-ray Diffraction Analysis.** XRD patterns were recorded on a Rigaku SmartLab X-ray diffractometer equipped with a 9 kW  $\text{CuK}\alpha$  rotating anode (operating at 40 kV and 150 mA) and D/teX Ultra 1D detector set in X-ray fluorescence reduction mode. The diffraction patterns were collected at room temperature in Bragg–Brentano geometry over an angular range  $2\theta = 15\text{--}80^\circ$ , with a step size of  $0.02^\circ$ . XRD data analysis was carried out using PDXL 2.1 software from Rigaku.

**Time of Flight Secondary Ion Mass Analysis (TOF-SIMS).** TOF-SIMS was performed using a newly develop TOF-SIMS for ToFwerk (Germany) mounted on a dual beam (focused ion beam and electron beam, Tescan Lyra 3 (Czech Republic)). A  $\text{Ga}^+$  beam at 30 kV was used for the TOF-SIMS measurement and only positive ion was measured.

**Brunauer–Emmett–Teller (BET) Measurements.** Specific surface area measurements were carried out by nitrogen physisorption at 77 K in a Quantachrome equipment, model autosorb iQ. The specific surface areas were calculated using the multipoint BET (Brunauer–Emmett–Teller) model, considering 11 equally spaced points in the  $P/P_0$  range from 0.05 to 0.35. Prior to measurements, samples (50 to 200 mg in form of powder) were degassed for 1 h at  $30^\circ\text{C}$  under vacuum to eliminate weakly adsorbed species.

**Transmission Electron Microscopy (TEM).** High angle annular dark field images (HAADF) were acquired on a FEI Titan “cubed” microscope equipped with a CEOS probe corrector. The imaging conditions were 300 kV electron beam energy and a 21 mrad convergence semiangle, leading to 0.08 nm probe size. The acceptance semiangle of the annular detector was set to 50–160 mrad.

**Neutron Powder Diffraction (NPD).** Powder neutron diffraction (NPD) patterns were collected at C2 High Resolution Powder Diffractometer, NRU reactor, Chalk River Laboratories at room temperature conditions, using vanadium sample cans. The instrument is equipped with a 800-wire

position-sensitive detector covering a range of 80 degrees. A wavelength of 1.328 Å neutrons were used to measure the data in  $2\theta$  range from  $5^\circ$  to  $117^\circ$ , with a step size of  $0.1^\circ$ . The data were analyzed using FullProf Suite.<sup>24</sup> We performed the refinements using the following constraint:<sup>13</sup> (i) full occupancy of Fe in M2 sites and (ii) lithium occupancy calculated as  $\text{occ}(\text{Li}) = 1 - [2 \times \text{occ}(\text{Fe})]$ . No extra Li-vacancies were considered.<sup>15</sup>

**Electrochemical Measurements.** The 2032 coin-type cells (20 mm diameter and 3.2-mm thick) were assembled in a glovebox in a high purity argon atmosphere. The cell consisted of the cathode, Li metal anode, microporous membrane (Celgard 2400) separator, and a nonaqueous electrolyte of 1 M  $\text{LiPF}_6$  in ethylene carbonate (EC)/dimethyl carbonate (DMC) (1:1 v/v). The cells were cycled at  $25^\circ\text{C}$  between 2.0 and 4.0 V vs  $\text{Li}^0/\text{Li}^+$  at constant current on a battery cycler. About the calculation of the capacity, we considered 89% of active material as composed by pure  $\text{LiFePO}_4$ , and then some capacity underestimation was possible.

**Calculation Method.** Our density functional theory calculation is performed using the VASP package<sup>25</sup> with the Project augmented wave function framework<sup>26,27</sup> and Perdew–Burke–Ernzerhof exchange–correlation functional.<sup>28</sup> A Hubbard U correction with a value of 3.7 eV is added to the d-electrons on Fe atoms, as suggested by Zhou et al.<sup>29</sup> All structures are relaxed until the maximum forces on the atoms are less than 0.01 eV/Å. The solvation free energies of  $\text{Ca}^{2+}$  and  $\text{Fe}^{2+}$  are adopted from Markus.<sup>30</sup>

## ■ ASSOCIATED CONTENT

### ■ Supporting Information

The Supporting Information is available free of charge on the ACS Publications website at DOI: 10.1021/acs.nanolett.6b00334.

HR(S)TEM and EDS images, XRD patterns, TOF-SIMS analysis, neutron powder diffraction pattern refinements, and electrochemical measurements (PDF)

## ■ AUTHOR INFORMATION

### Corresponding Author

\*E-mail: zaghib.karim@ireq.ca.

### Notes

The authors declare no competing financial interest.

## ■ ACKNOWLEDGMENTS

The authors want to acknowledge Prof. J. B. Goodenough of Texas University, Vincent Gariepy, Daniel Clement, Julie Trottier, and Catherine Gagnon of IREQ, Dr. Chandramohan George of Cambridge University, and Dr. Maria Filipousi of EMAT for helpful discussions. Z.F. would like to express his great thankfulness to Dr. Qi Shuai for the enlightening discussions. S.T. gratefully acknowledges the fund for scientific research Flanders (FWO) for a postdoctoral scholarship.

## ■ REFERENCES

- (1) Padhi, A. K.; Nanjundaswamy, K. S.; Goodenough, J. B. *J. Electrochem. Soc.* **1997**, *144*, 1188–1194.
- (2) Yang, S.; Song, Y.; Zavalij, P. Y.; Whittingham, M. S. *Electrochem. Commun.* **2002**, *4*, 239–244.
- (3) Wang, L.; He, X.; Sun, W.; Wang, J.; Li, Y.; Fan, S. *Nano Lett.* **2012**, *12*, 5632–5636.
- (4) Hsu, K.; Tsay, S.; Hwang, B. J. *J. Mater. Chem.* **2004**, *14*, 2690–2695.
- (5) Park, K. S.; Kang, K. T.; Lee, S. B.; Kim, G. Y.; Park, Y. J.; Kim, H. G. *Mater. Res. Bull.* **2004**, *39*, 1803–1810.
- (6) Wang, J.; Sun, X. *Energy Environ. Sci.* **2012**, *5*, 5163–5185.
- (7) Wang, J.; Sun, X. *Energy Environ. Sci.* **2015**, *8*, 1110–1138.
- (8) Chen, J.; Whittingham, M. S. *Electrochem. Commun.* **2006**, *8*, 855–858.
- (9) Qin, X.; Wang, J.; Xie, J.; Li, F.; Wang, X. *Phys. Chem. Chem. Phys.* **2012**, *14*, 2669–2677.
- (10) Cho, M. Y.; Kim, K. B.; Lee, J. W.; Kim, H.; Kim, H.; Kang, K.; Chul Roh, K. *RSC Adv.* **2013**, *3*, 3421.
- (11) Chen, J.; Bai, J.; Chen, H.; Graetz, J. J. *J. Phys. Chem. Lett.* **2011**, *2*, 1874–1878.
- (12) Chen, J.; Graetz, J. *ACS Appl. Mater. Interfaces* **2011**, *3*, 1380–1384.
- (13) Jensen, K. M. Ø.; Christensen, M.; Gunnlaugsson, H. P.; Lock, N.; Bøjesen, E. D.; Pro, T.; Iversen, B. B. *Chem. Mater.* **2013**, *25*, 2282–2290.
- (14) Chung, S.-Y.; Choi, S.-Y.; Yamamoto, T.; Ikuhara, Y. *Angew. Chem., Int. Ed.* **2009**, *48*, 543–546.
- (15) Paoletta, A.; Bertoni, G.; Hovington, P.; Feng, Z.; Flacau, R.; Prato, M.; Colombo, M.; Marras, S.; Manna, L.; Turner, S.; et al. *Nano Energy* **2015**, *16*, 256–267.
- (16) Franolet, M. *Bull. Soc. Fr. Miner. Cristal.* **1972**, *100*, 198–207.
- (17) Gauthier, M.; Michot, C.; Ravet, N.; Duchesneau, M.; Dufour, J.; Liang, G.; Wontcheu, J.; Gauthier, L.; Macneil, D. D. *J. Electrochem. Soc.* **2010**, *157*, A453–A462.
- (18) Wang, J.; Yang, J.; Tang, Y.; Liu, J.; Zhang, Y.; Liang, G.; Gauthier, M.; Chen-wiegart, Y. K.; Banis, M. N.; Li, X.; et al. *Nat. Commun.* **2014**, *5*, 4415.
- (19) Amisse, R.; Sougrati, M. T.; Stievano, L.; Davoisne, C.; Draz, G.; Budic, B.; Dominko, R.; Masquelier, C. *Chem. Mater.* **2015**, *27*, 4261–4273.
- (20) Dokko, K.; Koizumi, S.; Shiraishi, K.; Kanamura, K. J. *Power Sources* **2007**, *165*, 656–659.
- (21) Murugan, A. V.; Muraliganth, T.; Manthiram, A. J. *J. Phys. Chem. C* **2008**, *112*, 14665–14671.
- (22) Lee, K. T.; Kan, W. H.; Nazar, L. F. *J. Am. Chem. Soc.* **2009**, *131*, 6044–6045.
- (23) Boyang, H.; Guohua, T. J. *J. Mater. Chem. A* **2015**, *3*, 20399–20407.
- (24) Rodriguez-carvajal, J. *Phys. B* **1993**, *192*, 55–69.
- (25) Kresse, G.; Furthmüller, J. *Phys. Rev. B: Condens. Matter Mater. Phys.* **1996**, *54*, 11169–11186.
- (26) P E, B. *Phys. Rev. B: Condens. Matter Mater. Phys.* **1994**, *50*, 17953–17979.
- (27) Kresse, G.; Joubert, D. *Phys. Rev. B: Condens. Matter Mater. Phys.* **1999**, *59*, 1758–1775.
- (28) Perdew, J. P.; Burke, K.; Ernzerhof, M. *Phys. Rev. Lett.* **1996**, *77*, 3865–3868.
- (29) Wang, L.; Zhou, F.; Meng, Y. S.; Ceder, G. *Phys. Rev. B: Condens. Matter Mater. Phys.* **2007**, *76*, 165435.
- (30) Marcus, Y. J. *J. Chem. Soc., Faraday Trans.* **1991**, *87*, 2995–2999.